

Investigating the HD139664 Star and Debris Disk with ALMA

by

Aislinn Coleman-Plante

University of Colorado Boulder

Department of Astrophysical and Planetary Sciences

Defended April 1, 2024

Thesis Advisor:

Prof. Mark Rast, Department of Astrophysical and Planetary Sciences

Committee Members:

Prof. Paul Hayne, Department of Astrophysical and Planetary Sciences

Prof. Noah Finkelstein, Department of Physics

Prof. Meredith MacGregor, Johns Hopkins University, Department of Physics & Astronomy

(ex-officio)

This thesis entitled:

Investigating the HD139664 Star and Debris Disk with ALMA

Written by Aislinn Coleman-Plante

has been approved for the Department of Astrophysical & Planetary Sciences

Prof. Mark Rast

Prof. Paul Hayne

Prof. Noah Finkelstein

Prof. Meredith MacGregor

Date _____

The final copy of this thesis has been examined by the signatories, and we find that both the content and the form meet acceptable presentation standards of scholarly work in the above mentioned discipline.

Coleman-Plante, Aislinn (B.A., Astrophysics)

Investigating the HD139664 Star and Debris Disk with ALMA

Thesis directed by Prof. Meredith MacGregor, Johns Hopkins University, Dept. of Physics & Astronomy

Abstract

We present a comprehensive analysis of the HD139664 star and its debris disk, utilizing approximately 1.5 hours of data from the Atacama Large Millimeter/submillimeter Array (ALMA). HD139664, an F-type main sequence star located 17.5 parsecs from Earth, is surrounded by a nearly edge-on debris disk. This study aims to refine our understanding of the disk's interesting structure and the star's activity at millimeter wavelengths.

Employing CASA tasks, `tclean`, `uvmodelfit`, and various pipelines, we have created a resolved image of the debris disk and detected seven small flares from the star. A notable brightness asymmetry on the disk's right side suggests an interesting dynamic process at play. Our analysis uses a Markov Chain Monte Carlo (MCMC) framework to quantify the disk's architecture. Initially focusing on symmetric models to establish a baseline, we intend to further explore any asymmetries or eccentricities with a more complex model.

The findings from this study not only increase our knowledge of the specific HD139664 system but also contribute to the broader understanding of debris disks and stellar flares, and thus also the formation, evolution, and potential habitability of planetary systems.

Dedication

To all the stars that have inspired me, especially my new favorite, HD 139664. To all of my professors, who made me fall in love with astronomy, and finally, to my mom, for her unwavering support.

Acknowledgements

I would like to thank my advisor, Meredith MacGregor, who has mentored me from the beginning of my astronomy career during covid, and through this project, and most importantly helped me realize my dreams of pursuing research.

Thank you, Jay Chittidi, for always being willing to help and making me feel so welcome in our research group. Also thank you to Kiana Burton, who provided and helped me with the flare pipeline.

Contents

Chapter

Abstract		2
1 Introduction		8
2 Literature Review		10
2.1 Stellar Flare Model		10
2.2 Debris Disks		12
2.3 Previous work on HD 139664		14
3 Observations with ALMA		16
4 Data Analysis		18
4.1 CASA		18
4.2 Fitting a Disk Model		19
4.3 Identifying Flares		21
5 Results & Discussion		23
5.1 Best Fit Disk Model		23
5.1.1 Deprojected Visibilities		26
5.2 Flare Measurements and Interpretations		28
5.3 Uncertainties and Limitations		32
5.4 Future Work		33
6 Conclusions		34
Bibliography		35

Tables

Table

5.1 Resulting Best Fit values of the Disk Model	24
5.2 Flare Measurements	29

Figures

Figure

2.1 Standard Model for Stellar Flares	11
4.1 <code>tclean</code> Image of HD 139664	18
5.1 Model Image of Debris Disk	25
5.2 Corner plot of Disk Model Parameters	26
5.3 Deprojected visibilities Plot	27
5.4 Exposure Phases of Observed Flares	30

Chapter 1

Introduction

Debris disks are remnants of the planet formation process, acting as celestial analogues to our own Kuiper Belt. Composed of leftover dust from collisions between planetesimals, these disks are not only evidence of successful planet formation but also provide insight into the planetary systems in which they exist. The structure and location of debris disks can reveal the presence of possible exoplanets, particularly those located farther out in the system which cannot be detected by the common transit method, which is only sensitive to giant planets orbiting close to their host stars. Importantly, the millimeter-sized dust grains within these debris disks emit thermal radiation, which can be observed by ALMA. This observation offers a unique window into the complex dynamics of distant planetary systems.

HD 139664 is an F-type (F5 V) main sequence star located 17.5 parsecs from Earth and features a nearly edge-on debris disk. It is positioned within the southern constellation of Lupus and has an apparent magnitude of 4.64.

This project uses ALMA observations to further refine the structural details of this disk. Additionally, we aim to detect, measure, and characterize millimeter (mm) wavelength flares from the central star.

We Used the Common Astronomy Software Application (CASA) `tclean` algorithm to create a resolved image of HD139664 disk and star at mm wavelengths where, on the right hand side we see evidence of a potential brightness asymmetry in the disk, with a higher flux towards the top of the ansa.

In our research, we use a Markov Chain Monte Carlo (MCMC) Framework to delineate the characteristics of the disk, including its inner and outer radii, stellar flux, total disk flux, power-law index, inclination angle, position angle, and right ascension and declination offsets. So far we have been running symmetric models to constrain the initial starting parameters before we account for any asymmetries or eccentricity.

We also use the CASA `uvmodelfit` task to identify flares from the central star, of which we found 7 above the 3 sigma noise threshold.

Chapter 2 discusses relevant concepts associated with debris disks and stellar flares, and describes prior research that has been done on HD139664. Chapter 3 details ALMA's observational techniques. Chapter 4 covers the data analysis using CASA, our disk model, flare identification methodology, and preliminary results. Chapter 5 examines the implications of these findings, addresses the study's limitations, and outlines the next steps for this research. Chapter 6 summarizes the study's context and conclusions.

Chapter 2

Literature Review

2.1 Stellar Flare Model

Solar flares are observable across the entire electromagnetic spectrum and are believed to mirror processes occurring in stars throughout the universe. With the Sun, we have the ability to study the intricate dynamics of magnetic fields. Below, I will detail this process and its implications beyond our solar system.

The standard model of solar flares describes them as unpredictable releases of energy resulting from a particular kind of magnetic reconnection of features within the Sun's magnetic field [1]. This understanding was developed on our sun, but so far extends to stars of all spectral types. The Sun's magnetic field extends through its surface, or photosphere, far into the atmosphere, or corona, forming arches that return to the surface at "footpoints," tracing a pattern known as "coronal loops". In this flare model, electrons from the photosphere travel along these arched field lines into the corona, where they become polarized while spiraling around the lines. Magnetic field lines can twist and stretch due to the movement of plasma at the footpoints. When sufficiently stressed, the magnetic field lines may break and reconnect, transforming the coronal loops into a shorter arch, with the remainder forming a loop system that is disconnected from the Sun. This new configuration holds less magnetic energy and is closer to a potential field state. The energy released during this process accelerates electrons in various directions, leading to the emission of electromagnetic radiation from both thermal and non-thermal processes. Flares emit different wavelengths due to diverse radiation mechanisms. Electrons accelerated to near-light

speeds by magnetic fields, in a process where their acceleration is perpendicular to their initial velocity, generate synchrotron radiation, observed in radio and UV wavelengths from the tops of coronal loops [2]. For slower-moving charged particles, this process results in gyro-synchrotron radiation [3]. Additionally, when such electrons reach the flare's footpoints, they heat the plasma, leading to thermal radiation emissions, particularly in the infrared and optical spectrums.

Figure 2.1 illustrates the typical structure of a flare and the behavior of various wavelength regimes within this framework.

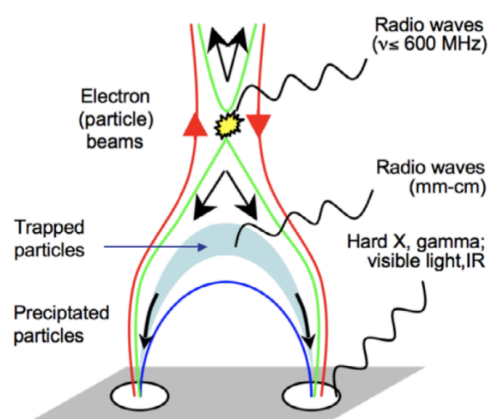


Figure 2.1: Multi-wavelength magnetic field structure and behavior [1].

This research presents the detection of millimeter wavelength flares on HD 139664, a sun-like F-type star. This wavelength regime has been largely overlooked in flare studies, with most prior research in the mm also only focused on M dwarf stars [4,5].

The discovery of mm flares on HD 139664, together with an increasing record of these events, indicates that flaring at these wavelengths might be a common characteristic among stars. This is supported by recent findings from a multiwavelength flare observation campaign on Proxima Centauri, which demonstrated a correlation between emissions in mm wavelengths and those in the far-ultraviolet (FUV) spectrum [6]. This correlation is critical for understanding the

mechanics of stellar flares and assessing the habitability of planetary systems orbiting active stars. The interaction between FUV and extreme ultraviolet (EUV) emissions with planetary atmospheres leads to significant chemical transformations and atmospheric escape, with high-energy stellar radiation altering and potentially heating exoplanetary atmospheres.

Moreover, while direct measurements of FUV and EUV stellar emissions are constrained to space-based observations, mm wavelength observations offer a promising alternative. Ground-based telescopes like ALMA can provide valuable insights into FUV activity, establishing a new avenue for assessing exoplanet habitability.

2.2 Debris Disks

During the early stages of star formation, circumstellar material is characterized by a high gas-to-dust ratio. This phase evolves over time, transforming from a protoplanetary disk, experiencing accretion, photoevaporation, stellar winds, and the formation of large solid bodies, into a more complex system. Debris disks, which emerge as a later stage in the planetary formation process, serve as evidence of the successful formation of planetary bodies ranging in size from hundreds to thousands of kilometers. These disks require a continuous supply of material through a collisional cascade process, where planetesimals are progressively ground down into dust grains [7]. This dust is primarily observable through scattered light and thermal emission.

Only debris disks within a few hundred parsecs of the sun are observable, due to their general faintness, but with the increasing discovery of planets in other systems, we assume debris disks are very common [8]. We consider any observed debris disks analogous to our Kuiper Belt, though on a much larger scale due to their faintness. These Kuiper Belt Analogs contain cold

dust, feature longer collisional timescales, and tell us about the orbital evolution during the latter stages of planet formation.

Surprisingly, the identification of debris disks is linked more closely to the disk's optical depth than to the age of the stellar system, optical depth being defined by the fractional luminosity of the disk relative to the star. Debris disks are characteristically optically thin across all wavelengths.

There is a dichotomy between broad and narrow populations of disks. Narrow disks are characterized by more defined and concentrated distributions of dust. They have commanded more attention because they are nice examples of planetary sculpting, where planetary bodies within these disks can gravitationally shape the surrounding debris, forming rings and gaps [7].

Broad disk systems are much more complex, with various theories suggesting different mechanisms for potential structures that remain unresolved. Broad disks are often associated with self-stirring or delayed-stirring mechanisms. This process involves the disk's own planetesimals growing to sizes where they have enough gravitational influence to stir the disk, leading to increased collisions and dust production. The distribution of growing planetesimals can be widespread, potentially leading to the formation of very broad debris disks. This process is not necessarily dependent on the presence of a large, fully formed planet, making it a plausible explanation for broad disks that do not show clear signs of planetary sculpting [9].

Debris disks can also display asymmetries, with eccentricity being particularly relevant in our study of HD 139664. Mechanisms disrupting the star-disk system's natural symmetry could be the influence of eccentric planets, interactions between dust and gas, or the result of recent large collisions [7].

We use observations of inclination and position angle to characterize debris disks. The inclination of a debris disk is the angle between the line-of-sight of the observer and the normal vector of the disk. At 0° inclination, the disk would appear face on, where a 90° inclination would be an edge-on view. The disk position angle is the angle between the north direction in the sky and the major axis of the disk, measured from north towards east: for example, a horizontal debris disk, as viewed in the sky from Earth, would have a position angle of 90° .

2.3 Previous work on HD 139664

A previous study in 2006 using the Hubble Space Telescope provided scattered light imagery of the debris disk surrounding HD 139664 [10]. However, these observations did not detect the brightness asymmetries that have been revealed in our analysis of the disk using ALMA data. They averaged the disk's two sides to enhance the signal-to-noise ratio and conducted simulations of scattered light disks to quantify the inner and outer disk radii, as well as radial and vertical dust density distribution. Their findings indicated a disk inner radius commencing at 60 AU, a dust concentration peaking at 83 AU, and a sharply defined outer edge at 109 AU. They were unsure about the dust-free zone within 60 AU, hoping future observations could confirm that.

The way dust scatters and emits light changes with the wavelength, and different wavelengths are suited to different sized dust grains, so discrepancies between our results and those of other studies are expected. At visible and infrared wavelengths observed by Hubble, we see light that has been scattered or reflected by dust particles, which is more sensitive to smaller dust grains. The millimeter and submillimeter wavelengths observed by ALMA show thermal emission from the dust itself and are ideal for picking up emissions from the larger and colder

dust grains and gas molecules that do not emit strongly at visible or infrared wavelengths. Larger, millimeter-sized grains are more effective in mapping the disk's dynamics, as these grains often mimic the movements of larger bodies like planetesimals [11].

Chapter 3

Observations with ALMA

ALMA is an interferometer which offers high-resolution imaging capable of resolving fine details, especially at mm and sub mm wavelengths, by combining signals from multiple antennas, whereas single-dish imaging provides wider fields of view with lower resolution. Interferometers work by sampling the visibility function, which is the Fourier transform of the sky brightness distribution. This method involves measuring $V(u,v)$, a function dependent on positions in the u - v plane, where u and v represent the vector separation between pairs of interferometers in units of wavelength. The spatial positioning of the antennas on the ground and the source's direction dictate where these samples are taken in the Fourier plane. During this observation with ALMA, only 42 out of the 66 antennas were used. The array's configuration dictates its capabilities: more extended arrays enhance spatial resolution, where more compact arrays improve sensitivity for larger sources. This observation used an array of 12-m antennas, featuring baselines up to 16 km.

The field of view of an interferometer is determined by the antenna size and the observing frequency, described through the "primary beam," indicating sensitivity. The synthesized beam size, which determines the resolution is 0.59×0.46 arcseconds.

This observation in Band 6 spans a wavelength range of 1.1 to 1.4 mm (equivalent to a frequency range of 272.5 to 214.1 GHz), and encompasses four spectral windows, each with a width of 1.875 GHz. Calibration of the absolute flux was achieved through observations of Titan.

These observations took place in 2016 over two sessions on May 13th and 15th, accumulating a total on-source time of 1.32 hours. Because interferometry depends on the spatial distance between each antenna, longer observations result in better data quality, as Earth's rotation allows different baselines to cover more visibility points and better sample the data.

When observing dust through thermal imaging or scattered light, we find that they are the most sensitive to grains of sizes about equal to the observing wavelength. Therefore, the millimeter wavelengths used in these observations are primarily imaging millimeter-sized dust grains [7].

Chapter 4

Data Analysis

4.1 CASA

We used CASA to create a resolved image of the HD139664 debris disk and star, make light curves, and manipulate the data. In this process, each point in the visibility plane represents a complex value indicating the amplitude and phase of the data, where amplitude correlates with the intensity of spatial frequencies, and phase indicates their location in the field of view.

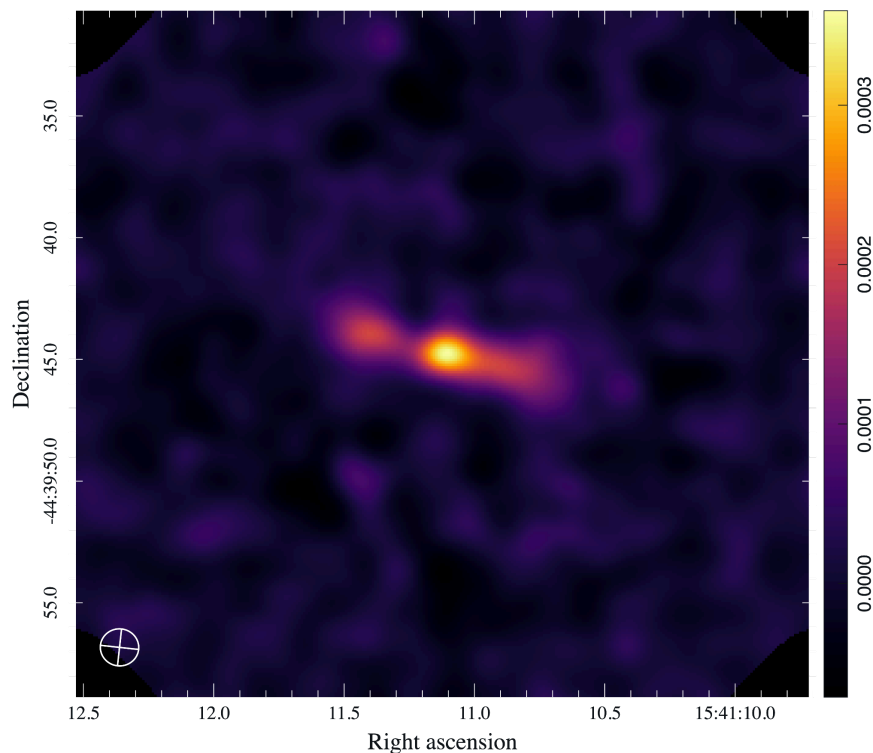


Figure 4.1: Image of HD 139664 generated with `tclean`, showing a protrusion on the upper right ansa of the disk, which indicates a possible asymmetry.

We used `tclean` for deconvolution and image generation, which iteratively reduces the flux from the brightest pixel within a specified region. Natural weighting was applied to give uniform weight to each visibility sample, prioritizing data points based on the natural density of samples in the $u-v$ plane. Additionally, a `uvtaper` of 1.4 was used to apply a Gaussian taper to the UV data weights, further improving surface brightness sensitivity and effectively "blurring" out the disk. In our flare analysis, further described in section 4.3, we used `uvmodelfit` to directly fit fluxes to the visibilities.

4.2 Fitting a Disk Model

To constrain the architecture of the disk, we fit the model directly to the visibilities using the modeling scheme described in MacGregor et al. 2013, 2015. This section will further explain the details of this methodology [12, 13].

The model code initially configures the parameters for generating a simulated astronomical image, including setting pixel size and number. To accurately simulate the observed size of the disk as seen from Earth, it converts from physical size at the system's distance to an angular size in radians.

Then, a function calculates the likelihood of a symmetric disk model given a set of parameters and observational data. Within this function, it sets up a series of model parameters: offsets in right ascension and declination, inner and outer radii of the disk, total disk flux, stellar flux, disk inclination, and position angle, along with a power-law index that describes the radial

distribution of the disk's material. We discerned the initial starting parameters from the image of HD139664 and applied noise to them.

The function then enforces several priors on these parameters to ensure they are within physically reasonable bounds. For example, the inner radius must not be negative or exceed the outer radius, and the total disk flux cannot be less than 0.

Next, the function constructs a grid representing the image space and applies transformations to account for the disk's inclination and position angle. This involves rotating the grid and calculating radial distances from the disk's center, taking into account the inclination to model the apparent shape and size of the disk correctly.

The disk image is generated by applying a power-law model to the radial grid, setting the brightness to zero outside the defined inner and outer radii, and a central point source, the star, is added to the image based on the specified stellar flux. The disk's surface brightness decreases with radius according to a power law, where the exponent, or power law index, reflects changes in the disk's temperature and material density from its inner to outer edges. A higher magnitude index suggests a sharper increase or decrease in both brightness and temperature, and a thinner distribution of material with distance.

Finally, the code calculates the chi-squared statistic between the generated model image and the provided observational data. To do this we use the `galario` package that converts the model image into synthetic visibilities, which involves array operations like fourier transforms and transpositions, taking into account properties of the specific ALMA array during my observation, such as resolution, sensitivity, and distribution of antennas [14]. Then it compares these synthetic visibilities with the observed visibilities, summing the chi-squared values from

each piece of data to obtain a total chi-squared value. The log likelihood is then calculated from the total chi-squared, which quantifies how well the model fits the data.

A key component of the model's process employs the `emcee` library for Bayesian inference using Markov Chain Monte Carlo (MCMC) simulations [15]. MCMC is a method for performing a random walk through parameter space to obtain a set of samples that accurately represent the distribution. The position of each point in a Markov chain is influenced solely by the location of the previous one. To modify a walker's position, another walker is selected at random from the group, proposing a new potential position. If this is rejected, the walker remains in its current position, and this process is repeated. The decision to accept or reject a step is governed by the Metropolis-Hastings Algorithm, which uses the acceptance ratio as its criteria. Over time, this algorithm converges towards a stationary collection of samples that reflects the underlying distribution.

By employing a model that simulates the appearance of these objects based on a set of physical parameters, MCMC iteratively navigates through many combinations of these parameters to probabilistically converge on the best fit to the observed data, while quantifying the uncertainties of these estimations.

4.3 Identifying Flares

To identify flares, we need to identify what is noise and what is flux from the star. To do this, we search for where the flux of the star has a significance of at least 3 times the root mean square (rms) noise level from the observation. The rms noise level is determined from parts of the data that do not contain the star or the surrounding debris disk. To compare the measured

noise level to the flare candidates and isolate those exceeding the 3σ threshold for the whole dataset, we used a python script first described in Kiana Burton et al. (2022) [16].

The pipeline uses the `uvmodelfit` task in CASA, which performs a simple chi-square fitting to the visibilities. After iterating through each integration time to identify the optimal flux density at each interval, It then generates a light curve for the entire dataset.

The observations had integration times of 6.05 seconds, consistent with the typical duration of observed mm flares, which are less than 30s. Although shorter integration times result in higher noise levels, they are useful for precisely determining the timing of events within the data.

We expect the noise across all scans to remain relatively constant, but in reality, the noise in some scans can be abnormally elevated due to factors such as the time of night the exposures were taken, an ‘antennae issue’, or contamination from stellar flaring emission. To mitigate this variability, the pipeline calculates a unified rms noise level for each scan. This is achieved by taking the three integrations showing the lowest flux densities, and averaging these values. The process involves using `tclean` to produce images for these scans and then determining the rms noise by examining only those regions without the source.

Finally, it flags any integration that has a flux density above 3 times the rms value for that scan as a potential flare.

Chapter 5

Results & Discussion

5.1 Best Fit Disk Model

In this model, we set the flux values for the star and the disk as constants at 0.00025 and 0.0015 Jy, respectively, derived using the CASA `uvmodelfit` task. We fixed these flux parameters to focus on fitting for the architecture of the disk. The model fits for five free parameters: the inner radius, outer radius, inclination, position angle, and power-law index, with the resulting values presented in table 5.1. Unlike previous iterations of the model, we did not treat disk and star offsets as variable parameters due to consistently negligible best-fit offsets within our resolution's limit, well below our synthesized beam size of 0.56×0.45 arcseconds. The generated model image is shown in figure 5.1.

The model's outcomes include an inner radius of 21.32 AU and an outer radius of 103.90 AU, indicating a substantial disk width of approximately 82 AU. This is quite broad, which is a particularly interesting result considering the dichotomy between broad and narrow disk populations discussed in Section 2.2, and could suggest the potential presence of unresolved substructures [9].

This finding diverges significantly from the inner radius estimated by Kalas et al. (2006), which estimated a value of approximately 60 AU [10]. This discrepancy is not unreasonable and can be attributed to the different sensitivities of Hubble and ALMA to various grain sizes, resulting in their imaging different regions of the disk.

We are still working on refining the flux fittings for the star and disk. Challenges exporting data from CASA have resulted in inaccuracies when these fluxes are allowed to vary. Future work will address these issues and consider fluxes as variable parameters. Additionally, given the disk's potential asymmetry, we plan to adjust the model to account for these irregularities, like eccentricity.

While this model is not yet complete, and extensive further modeling is planned, the findings reported here provide valuable insights into the disk's structure.

Table 5.1: Resulting Best Fit values of the Disk Model

Parameter	Description	Best-Fit	Confidence Interval
R_{in}	Inner Radius	21.32 AU	+1.49, -2.67
R_{out}	Outer radius	103.90 AU	+2.63, -2.07
Incl	Inclination angle	79.79°	+0.44°, -0.50°
PA	Position angle	76.29°	+0.49°, -0.50°
xx	Power law index	-0.66	+0.20, -0.13
Disk off RA	Disk right ascension offset	~0	+0.05, -0.05
Disk off Dec	Disk declination offset	~0	+0.05, -0.05

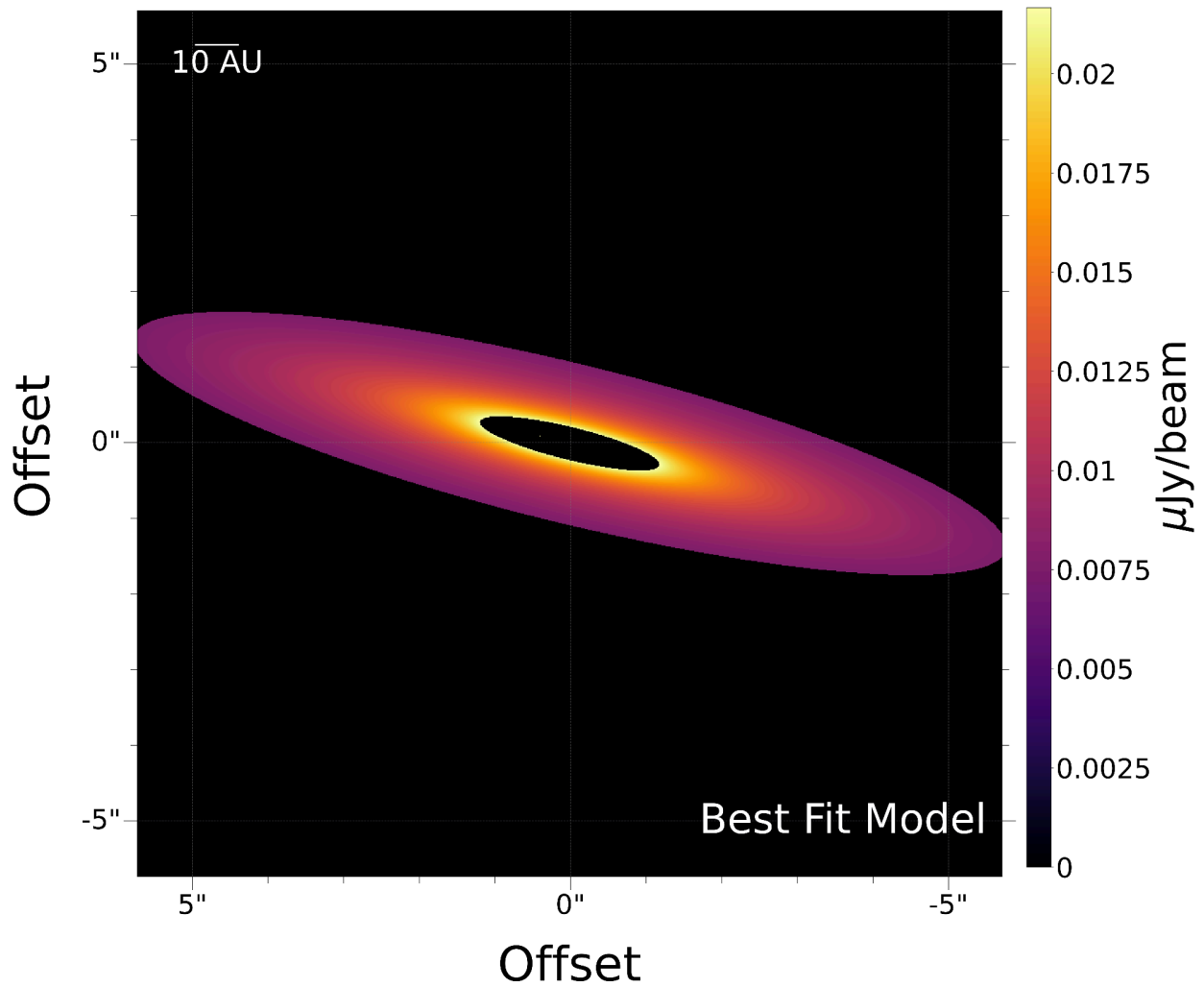


Figure 5.1: Model Image

The corner plot in figure 5.2 visualizes the results from this model with over 350,000 MCMC trials. On this plot, the diagonal panels feature 1D histograms representing the marginalized posterior probability distributions for each parameter, independent of the others. The peak of each histogram indicates the parameter's best-fit value. Surrounding panels display contour plots that map the 1σ , 2σ , and 3σ confidence regions for every pair of parameters, illustrating how they correlate with each other while also showing the uncertainties.

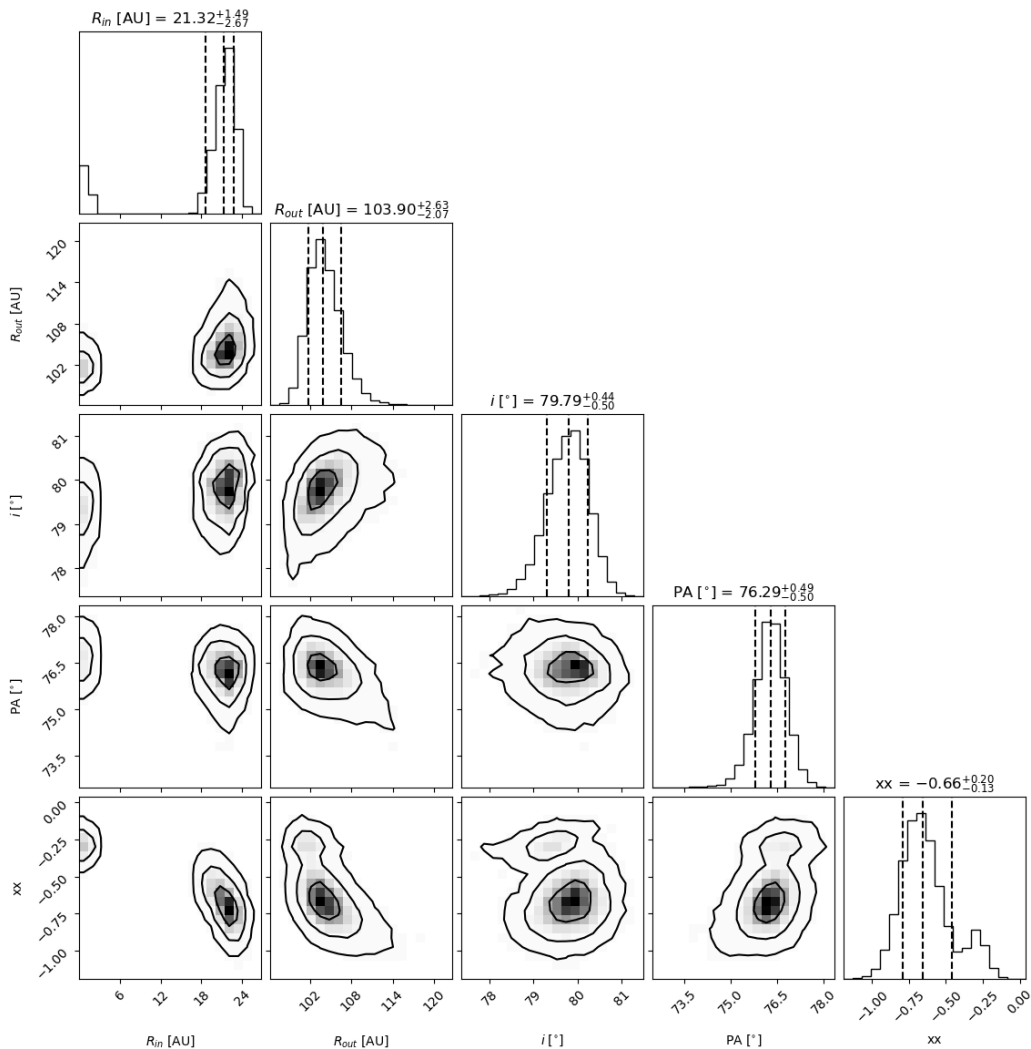


Figure 5.2: Corner plot showing parameter distributions and their correlations of the disk model.

5.1.1 Deprojected Visibilities

To gain a more straightforward interpretation of the underlying physical structures of the disk, we use the deprojected visibility function. This technique leverages the (near) axis symmetry of disks to simplify the complex visibility data collected by interferometers. By deprojecting and radially averaging the visibility data, we can effectively reduce the dimensionality of the data set [17].

In the context of a debris disk, we adjust the observed visibilities to account for the disk's inclination and position angles and average the real part of these complex visibilities in concentric annuli based on their deprojected (u,v) distance from the disk's center. For a simple isolated and uniformly bright disk, this method produces a profile that resembles a sinc function, which is a mathematical consequence of the properties of Fourier transforms, and ultimately helps us understand the spatial distribution of matter within the disk [17].

The real visibilities contain the flux information of the disk, and when plotted against the UV Distance, they show a peak corresponding to the total flux of the disk. This peak is then followed by a decline and subsequent ripples. Figure 5.3 shows a central peak at 0.0023 Jy, matching the total disk flux from `uvmodelfit`. However, unlike the traditional sinc function, the profile of my data will not dip below zero due to the star's point source influence.

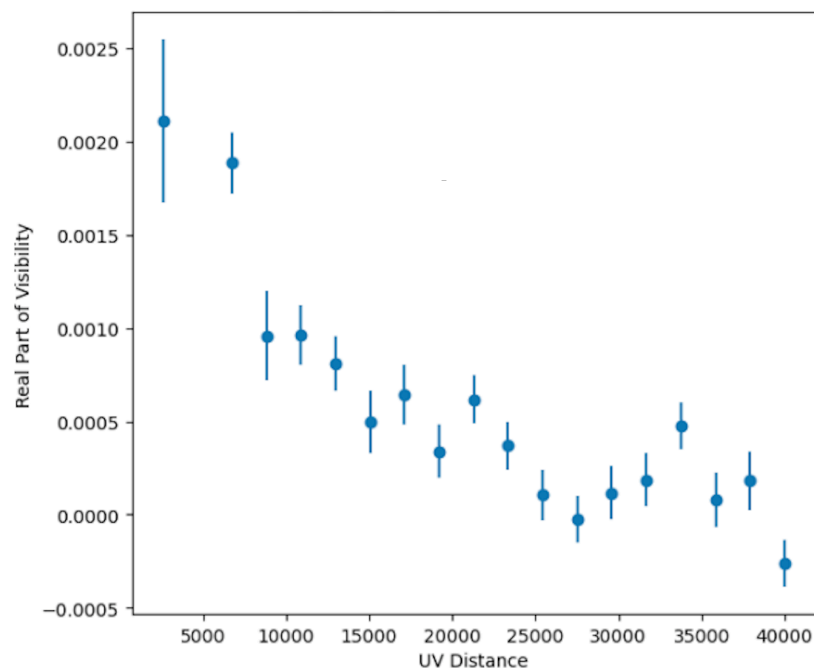


Figure 5.3: Deprojected visibilities plot, where the error bars represent the uncertainty in the weighted average value of the real and imaginary parts of the visibilities.

We applied this deprojected visibilities function to evaluate how well the data in this form aligns with the physical parameters of the disk. The characteristic sinc profile of this figure and the peak at our expected total disk flux confirms that the real part of these visibilities do reflect our expectations.

5.2 Flare Measurements and Interpretations

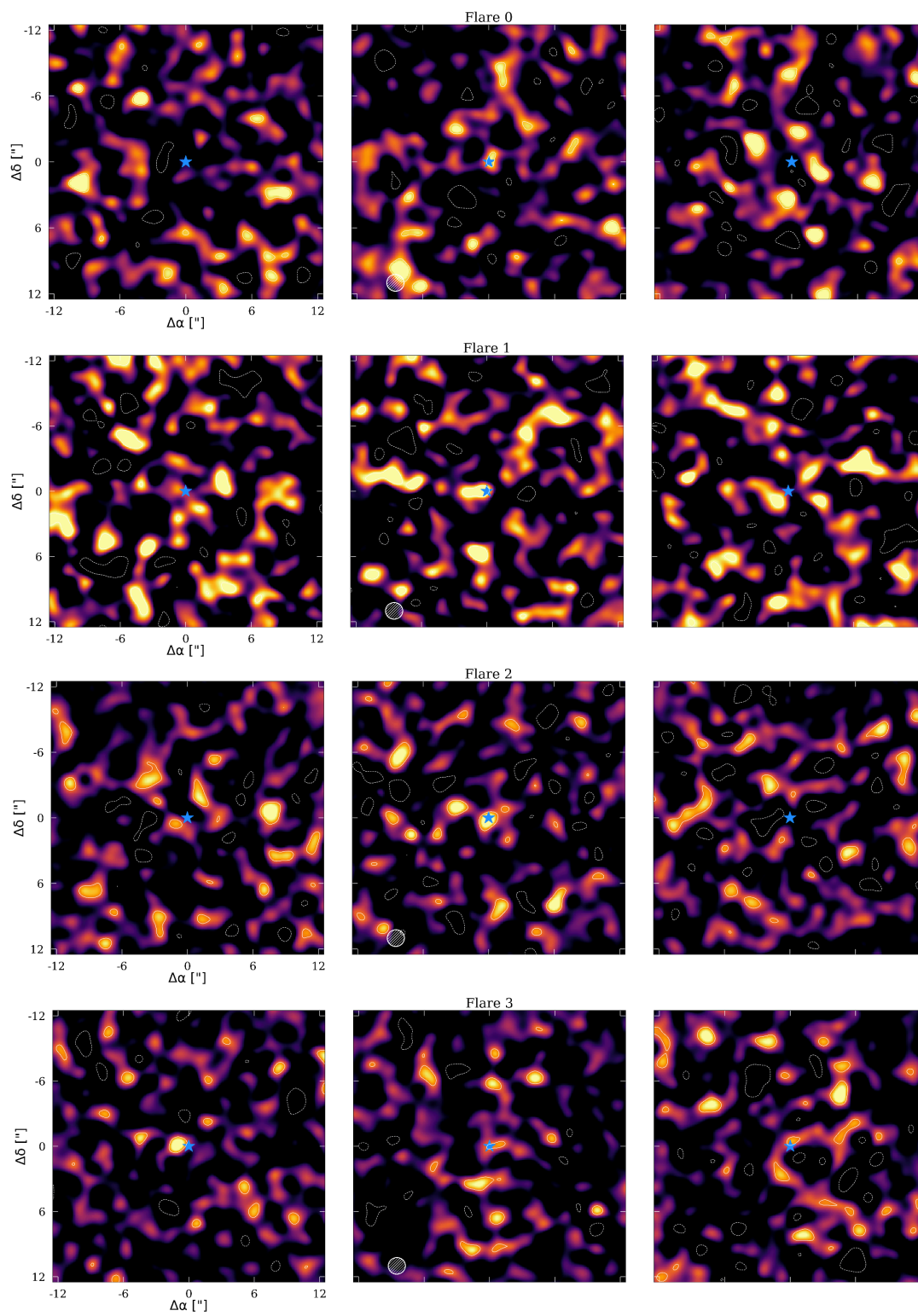
Using this pipeline, 7 flares were flagged as being above 3σ , whose measurements are detailed in table 5.2. Over 1.32 hours of on-source data collection, we identified 7 flares, corresponding to an average of approximately 5.3 flares per hour in band 6, or around 127 small flare events daily. While flare rates are typically compared within the same energy level and among stars of the same spectral type, most millimeter flare studies have concentrated on M-type stars and more energetic events. Our closest benchmark involves a similar-aged sun-like star, Epsilon Eridani [16]. Burton et al. 2022 observed this K-type star to experience roughly 3 flares every 4 hours at a magnitude of 30 mJy—30 times brighter than the flares we observed. The brighter nature of these flares implies a lower frequency for such intense events, which aligns with the expectation that larger magnitude flares occur less frequently, adhering to a power law distribution.

Table 5.2: Flare Measurements

	Luminosity [erg/s]	Significance	Flux Density [mJy]
Flare 0	4.93e+18	3.649	1.348 +/- 0.22
Flare 1	5.67e+18	3.453	1.548 +/- 0.22
Flare 2	3.94e+18	3.626	1.077 +/- 0.16
Flare 3	3.55e+18	3.261	0.969 +/- 0.16
Flare 4	3.55e+18	3.304	0.971 +/- 0.16
Flare 5	3.62e+18	3.368	0.989 +/- 0.16
Flare 6	4.02e+18	3.369	1.096 +/- 0.16

The primary beam of an ALMA antenna, exhibiting a Gaussian response profile that peaks at its center, is most sensitive at this central point, with sensitivity gradually decreasing towards the edges. This characteristic implies that genuine signals, such as flares detected near the center of the beam, are recorded with greater accuracy compared to those near the edges. Additionally, noise in these regions can sometimes mimic the intensity of weaker flares seen near the beam's center, owing to this sensitivity gradient.

We want to emphasize that all images in figure 5.4 have undergone a primary beam correction. This process adjusts the image by dividing it by the antenna's power response function, to improve flux density accuracy at the edge of the primary beam. However, while this correction "upweights" real signals, it also amplifies the noise near the image edges. To avoid this complication in our flux measurements, we used the aforementioned pipeline to fit a stellar flux directly to the visibilities.



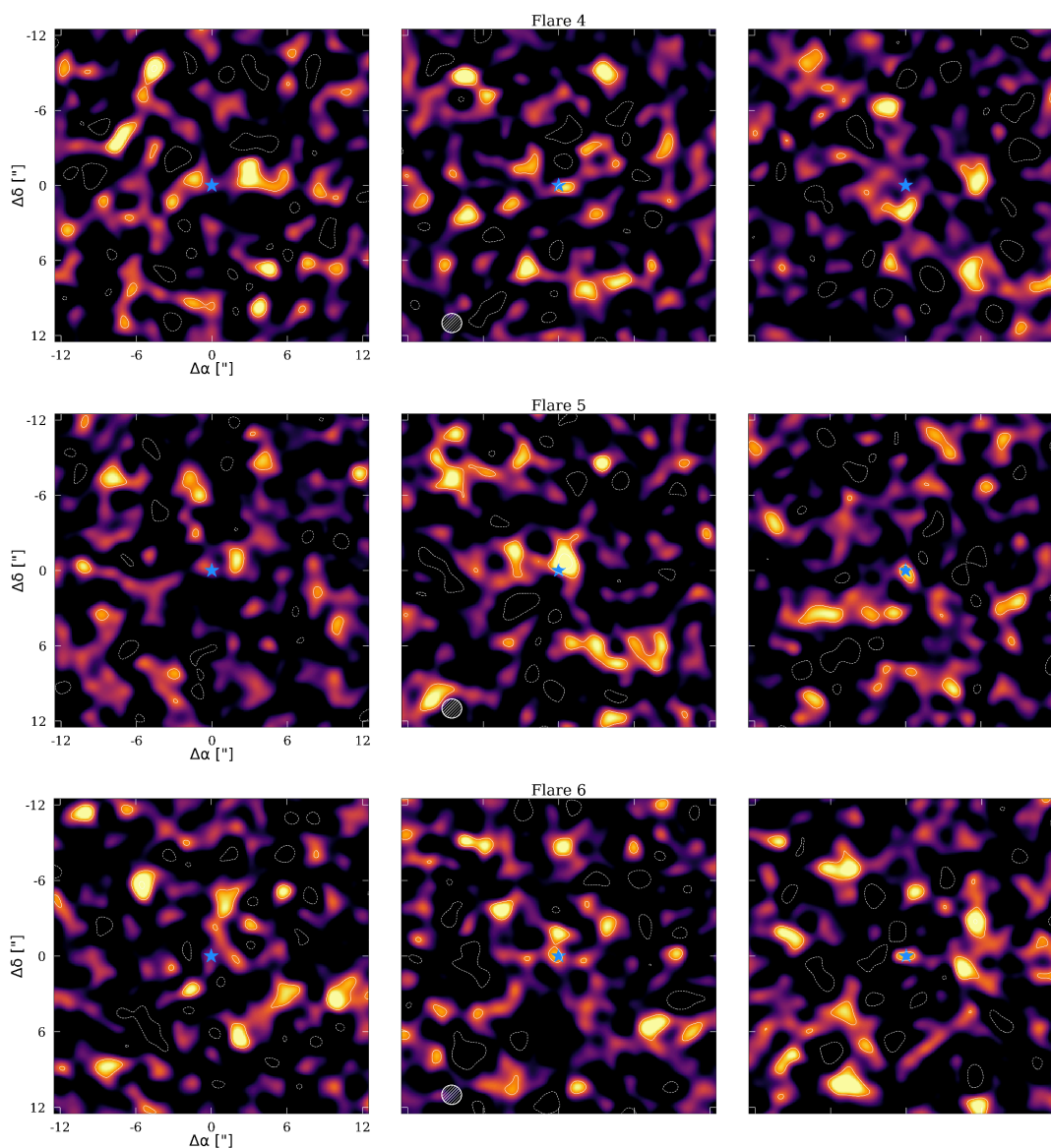


Figure 5.4: Each of these images shows a different 6.5 second exposure. The image on the left shows the exposure preceding the flare, the center image shows the flare's peak intensity, and the right hand image shows the exposure directly after the flare. Solid contours indicate the 3σ level, whereas dashed contours indicate the -3σ level.

Studies of disks at mm wavelengths have recently started paying more attention to the activity of the star, and the importance of disentangling dust and stellar emission. While many researchers have observed excess brightness from stars within these disks, they often attribute it

to unresolved inner dust belts heated by the star and glowing at mm wavelengths. The discovery that stellar flares, not unresolved inner dust, significantly contribute to millimeter-wavelength emissions shows the importance of studying both stellar and dust activities for a complete understanding of the disk's structure and the system as a whole [16].

5.3 Uncertainties and Limitations

Many uncertainties that inherently exist imaging such a distant object with any telescope. ALMA's flux calibration carries an overall uncertainty of 5%. There is also a level of uncertainty on each parameter in the model fits detailed in Table 5.1, along with uncertainties in the flare signals from `uvmodelfit`, which are listed in Table 5.2.

Using 6-second integration times for our observations could have smoothed over the peak intensities of flares, leading to underestimated flux measurements. This averaging can be significant for transient events like flares, which can vary significantly over short periods of time. Thus, our method may have systematically underrepresented the true flux of the peak of these flares.

A significant amount of our research effort was dedicated to configuring the data into the correct form for the disk model and debugging the disk model. This process proved to be more time-consuming than anticipated, due to the complexity of the data and the large scale of the models we are running. As a result, the constraints limited our ability to fit for the fluxes and also explore more complex models.

5.4 Future Work

We plan to continue our efforts to identify and resolve the issue causing the flux inaccuracies. The challenges exporting the data from CASA, which lead to inaccuracies when fluxes are treated as free parameters, is our main priority in this ongoing study. As we move forward, the star and disk flux will be reintroduced as variable parameters within our model framework to get a more holistic understanding of this disk.

Our main goal is to add to the model to account for the asymmetries we see in figure 4.1 in the right hand ansa of the disk. We suspect this disk could be eccentric which would involve fitting an eccentric model as described in MacGregor et al. 2017 [18]. This involves fitting for the orbital parameters of particles in the disk in addition to the structural parameters described in section 4.2 [19].

As described in section 2.2, various theories exist regarding the mechanisms that sculpt the extensive and potentially intricate structures of wide debris disks, yet there remains a lack of consensus. Given this context, the analysis of dynamics of another broad and unusual debris disk could contribute to a deeper understanding of these complex systems.

Chapter 6

Conclusions

This research uses 1.3 mm ALMA observations to do a comprehensive analysis of the HD 139664 debris disk and star. In the preliminary results of this ongoing study, we have constrained parameters in the architecture of this disk and made the notable discovery that this is a very broad debris disk of ~ 80 AU. Further modeling will be done to gain a more robust understanding of this disk and quantify the observed asymmetries. Beyond constraining the characteristics of HD 139664's debris disk, this study contributes to our understanding of wide debris disks and planet formation processes, helping us learn more about how planetary systems develop.

We also measured the first mm flares on an F type star, calculating an approximate rate of ~ 5 flares per hour for these low energy events. This discovery contributes to the increasing detections of millimeter flares and confirms their occurrence on F-type stars. Beyond broadening the scope of millimeter flare observations, this analysis also helps us constrain the structure of the disk, ensuring that this excess flux is not incorrectly attributed to unresolved inner dust.

Bibliography

- [1] Klein, K.-L., & Dalla, S. 2017, SSRv, 212, 1107
- [2] Massi, M. et al 2006, A&A, 453, 959
- [3] White, S. M., & Kundu, M. R. 1992, SoPh, 141, 347
- [4] Meredith A. MacGregor et al 2018 ApJL 855 L2
- [5] Meredith MacGregor et al 2020 ApJ 891 80
- [6] Meredith A. MacGregor et al 2021 ApJL 911 L25
- [7] Hughes, A. Meredith, Duchêne, Gaspard, & Matthews, Brenda C. 2018, ARA&A, 56, 541
- [8] Winn, J. N., & Fabrycky, D. C. 2015, ARA&A, 53, 409
- [9] Marino, S. 2021, MNRAS, 503, 5100
- [10] Paul Kalas et al 2006 ApJ 637 L57
- [11] M. C. Wyatt 2006 ApJ 639 1153
- [12] Meredith A. MacGregor et al 2013 ApJL 762 L21
- [13] Meredith A. MacGregor et al 2015 ApJ 809 47
- [14] Tazzari, M., Beaujean, F., & Testi, L. 2018, MNRAS, 476, 4527
- [15] Daniel Foreman-Mackey et al 2013 PASP 125 306
- [16] Kiana Burton et al 2022 ApJL 939 L6
- [17] O. P. Lay et al 1997 ApJ 489 917
- [18] Meredith A. MacGregor et al 2017 ApJ 842 8
- [19] M. C. Wyatt et al 1999 ApJ 527 918